

1 **Water vapor in Titan's stratosphere from Cassini/CIRS Far-infrared**
2 **spectra**

3
4 V. Cottini¹, C. A. Nixon^{1,2}, D. E. Jennings¹, C. M. Anderson¹, N. Gorius^{1,3}, G. L. Bjoraker¹,
5 A. Coustenis⁴, N. A. Teanby⁵, R. K. Achterberg^{1,2}, B. Bézard⁴, R. de Kok⁶, E. Lellouch⁴, P. G.
6 J. Irwin⁷, F. M. Flasar¹, G. Bampasidis^{4,8}

7
8 *¹Planetary Systems Laboratory, NASA Goddard Space Flight Center, Greenbelt, MD 20771,*
9 *USA, ²Department of Astronomy, University of Maryland at College Park, College Park, MD*
10 *20742, USA, ³Department of Physics, The Catholic University of America, Washington, DC*
11 *20064, USA, ⁴LESIA-Observatoire de Paris, CNRS, UPMC Univ. Paris 06, Univ. Paris-Diderot,*
12 *France, ⁵School of Earth Sciences, University of Bristol, Wills Memorial Building, Queen's*
13 *Road, Bristol BS8 1RJ, United Kingdom, ⁶SRON, Sorbonnelaan 2, 3584 CA Utrecht,*
14 *Netherlands, ⁷Atmospheric, Oceanic and Planetary Physics, University of Oxford, Oxford, OX1*
15 *3PU, UK, ⁸Faculty of Physics, National and Kapodistrian University of Athens, Athens, Greece*

16
17 Corresponding author:

18 Valeria Cottini,

19 Address: NASA/GSFC, Code 693, Bldg. 34, Rm. S121, 8800 Greenbelt Rd., Greenbelt, MD,
20 20771, United States

21 Office phone number: 001 301 286 7932

22 Email: valeria.cottini@nasa.gov

23

24 *Abstract*

25

26 Since the first detection of water vapor in Titan's stratosphere by disk-average observations from
27 the Infrared Space Observatory (Coustenis et al. 1998) we report here the successful detection of
28 stratospheric water vapor using the Cassini Composite Infrared Spectrometer (CIRS, Flasar et al.
29 2004). CIRS senses water emissions in the far infrared spectral region near 50 microns, which
30 we have modeled using two independent radiative transfer codes (NEMESIS, Irwin et al 2008
31 and ART, Coustenis et al. 2007, 2010). From the analysis of nadir spectra we have derived a
32 mixing ratio of (0.14 ± 0.05) ppb at an altitude of 97 km, which corresponds to an integrated
33 (from 0 to 600 km) surface normalized column abundance of $(3.7 \pm 1.3) \times 10^{14}$ molecules/cm². In
34 the latitude range 80°S to 30°N we see no evidence for latitudinal variations in these abundances
35 within the error bars. Using limb observations, we obtained mixing ratios of (0.13 ± 0.04) ppb at
36 an altitude of 115 km and (0.45 ± 0.15) ppb at an altitude of 230 km, confirming that the water
37 abundance has a positive vertical gradient as predicted by photochemical models (e.g. Lara et al.
38 1996, Wilson and Atreya 2004, Horst et al. 2008); retrieved scaling factors (from ~ 0.1 to ~ 0.6)
39 to the water profile suggested by these models show that water vapor is present in Titan's
40 stratosphere with less abundance than predicted.

41

42 *1. Introduction*

43

44 Water is present in its various forms in many regions of the solar system, from the atmospheres
45 of the inner planets and shadows of lunar craters, to the mantles of icy satellites and beyond to
46 the Kuiper Belt Objects (KBOs) and Oort Cloud Comets. Liquid water is also an essential

47 ingredient for life on Earth and a potential clue in the search for life or habitability conditions in
48 the rocks of Mars, the internal ocean of Europa or Titan, and the volcanic vents of Enceladus. On
49 Titan, Saturn's largest satellite that hosts a dense nitrogen-dominated atmosphere, water is a trace
50 species in the stratosphere. However, water plays a significant role since it is one of the sources
51 of oxygen for the observed active photochemistry on Titan (e.g. Lara et al. 1996, Wilson and
52 Atreya 2004, Horst et al. 2008).

53 Titan's known oxygen compounds to date are carbon monoxide (CO, ~47 ppm), carbon dioxide
54 (CO₂, ~15 ppb) and water vapor (H₂O), where the abundances are quoted for the low-latitude
55 stratosphere (de Kok et al. 2007a). CO₂ was first detected by Voyager 1 (Samuelson et al. 1983),
56 while CO was first seen by ground-based observations in the near-IR (Lutz et al. 1983).
57 Subsequent observations in the sub-millimeter led to controversy as to whether CO was well-
58 mixed or not (Hidayat et al. 1998, Gurwell et al. 2004). CO emission lines were later observed
59 by Cassini/Composite Infrared Spectrometer (CIRS), thus improving the previous abundance
60 estimate (de Kok et al. 2007a, Teanby et al. 2009). Water was detected at a mixing ratio of 0.4
61 ppb, assumed to be uniform above the condensation level, by two lines near 40-micron observed
62 in Short Wavelength Spectrometer (SWS) spectra acquired by the Infrared Space Observatory
63 (ISO) in 1997 (Coustenis et al. 1998). An early attempt to measure it with Cassini CIRS was
64 unsuccessful due to poorer signal-to-noise (S/N) ratios in early versions of the calibration
65 pipeline spectra and fewer spectra were available. Therefore, only an upper limit of 0.9 ppb
66 could be retrieved (de Kok et al. 2007a). Since then, water emission in CIRS data have been
67 definitely observed, albeit without deriving any further information on its abundance and
68 distribution (Bjoraker et al. 2008).

69 While the presence of these oxygen compounds is now well-established, the question of their
70 origin remains controversial. Early photochemical models assumed that CO originated from
71 episodic outgassing from Titan's interior along with nitrogen (N_2) or ammonia (NH_3) and
72 methane (CH_4), whereas water molecules entered the top of the atmosphere and photochemically
73 produced oxydryl radicals (OH) (Wong et al. 2002; Wilson and Atreya 2004). The combination
74 of OH and CO led to the production of CO_2 . However, Horst et al. (2008) have recently
75 challenged this model, arguing instead that both CO and CO_2 are the result of upper-atmospheric
76 chemistry which occurs between in-falling oxygen species reacting with carbon produced by
77 CH_4 photodissociation. In this hypothesis, water enters Titan's atmosphere either in the form of
78 H_2O or OH (since the latter is quickly converted to H_2O within the atmosphere) together with
79 atomic oxygen (O and O^+). These forms of oxygen are deposited at two different altitudes on
80 Titan. The O^+ ions are deposited in the upper atmosphere around 1100 km (Hartle et al. 2006a,b)
81 where their interaction with methyl (CH_3) radicals leads to the formation of CO. Water is instead
82 deposited at 750 km due to micrometeoritic ablation (English et al. 1996) where it is photolyzed
83 to OH. The latter finally combines with CO to form CO_2 and possibly other complex species.
84 Saturn's rings and the icy satellites that surround the giant planets, and also interplanetary dust,
85 are probable sources of the water (oxygen) in Titan's atmosphere and recent results from the Ion
86 and Neutral Mass Spectrometer and magnetometer on board Cassini indicate that the plumes of
87 Enceladus are the dominant source (e.g. Dougherty et al. 2006). Based on Herschel
88 measurements of the Enceladus torus combined with modeling of the fate of the species within
89 the torus, Hartogh et al. (2011) showed that the flux of O / O^+ into Titan is consistent with an
90 Enceladus source for the oxygen seen in Titan CO, except for the fact that Enceladus does not
91 seem to provide enough OH/ H_2O . Characterizing the occurrence of these oxygen species has

92 important implications for understanding the origin and evolution of Titan and the synthesis of
93 the complex molecules found in its atmosphere.

94 In this paper, we analyze the spectra acquired by CIRS in the far infrared spectral region in order
95 to retrieve the water vapor verticals or spatial distribution in Titan's atmosphere. CIRS has been
96 acquiring spectra of Titan since the beginning of the Cassini prime mission (July 2004). After
97 two years of the extended mission (XM), which included the 2009 equinox, in July 2010 Cassini
98 entered in the Solstice Mission (SM), which will last until 2017. Since the upper limit to H₂O
99 was reported by de Kok et al. (2007) there has been a considerable increasing of the number of
100 data collected by CIRS during the length of the mission and significant improvements to their
101 calibration. The increased signal to noise (S/N) ratio not only permits a definitive detection of
102 H₂O from the analysis of CIRS far infrared spectra, but it allows us to constrain its vertical and
103 latitudinal profile.

104

105 *2. Selected dataset*

106

107 CIRS (Flasar et al. 2004) is comprised of three Focal Planes observing in the spectral range 10 -
108 1400 cm⁻¹ with spectral resolutions from 0.5 to 15.5 cm⁻¹. Focal Plane 1 detector (FP1) is
109 characterized by a circular field of view of 3.9 mrad. It records data in the far infrared spectral
110 range (10 – 600 cm⁻¹) with a spectral resolution of 0.5 cm⁻¹, allowing us to observe the water
111 vapor signature, and by modeling, to retrieve its abundance. Water presents its rotational lines in
112 the CIRS FP1 spectral region up to 400 cm⁻¹, with the strongest and most visible lines in the
113 range positioned between 90 and 260 cm⁻¹. We focus here on the range from 150 to 260 cm⁻¹ for
114 the water detection, as this is the range of maximum responsivity of FP1. At lower wavenumbers

115 the on-board electronics of CIRS create a moving interference spike that can affect the spectrum
116 up to 150 cm^{-1} . Therefore, we exclude wavenumbers shorter of 150 cm^{-1} . We use data from two
117 different types of observations to obtain independent measurements: the far infrared on-disk
118 integrations (FIRNADCMP) and the far infrared limb integrations (FIRLMBINT). Water is a
119 trace species with relatively weak lines and therefore it cannot be observed in an individual
120 spectrum. An average of a few thousand spectra of on-disk observations and a few hundred
121 spectra of limb observations is necessary to achieve sufficient signal-to-noise (Figure 1).

122 Limb observations have the FP1 focal plane centered around two different altitudes – hereafter
123 limb 1 and 2 – and are therefore used to constrain water vapor abundance in the stratosphere,
124 around 115 and 230 km respectively, well above the tropopause. Since the contribution functions
125 of water for on-disk observations peak around 97 km (Figure 2), the retrieved water vapor
126 abundance derived from these measurements can be compared with the lowest altitude targeted
127 by our limb integrations around 115 km.

128 For the water detection and retrieval of quantitative information together with possible latitudinal
129 variations, multiple Titan flybys must be utilized to enhance the signal. To date, 35 limb
130 integrations of approximately 1 hour in duration (~60 high-resolution spectra) have been
131 obtained covering latitudes from 87°S to 80°N . The nadir integrations are more numerous (about
132 92 successfully executed, of typical duration 5 hrs, ~300 spectra) as they occur in a less
133 contested observing time further from the desirable Titan closest-approach period; they have
134 more or less complete spatial coverage of Titan's latitudes and longitudes with an average
135 footprint size of $\sim 15^{\circ}$ great circle arc.

136 We focus on one season of on-disk observations acquired from December 2004 to December
137 2008 (northern winter on Titan) in order to reach a compromise between obtaining a large

138 number of spectra and a sufficiently homogeneous dataset. Inside this time period for on-disk
139 observations acquired from a maximum distance of 300,000 km and with a maximum emission
140 angle of 60° , we selected latitudinal bins ($80^\circ\text{S} - 45^\circ\text{S}$), ($45^\circ\text{S} - 10^\circ\text{S}$), and ($0^\circ - 30^\circ\text{N}$) centered
141 around three latitudes for which observation-derived temperature profiles were available (see
142 model description in section 3). The numbers of spectra averaged in these latitudinal bins were
143 respectively around 1700, 3800 and 7000 and their average emission angles were respectively
144 35° , 38° and 34° .

145 CIRS limb spectra are acquired in much smaller numbers, therefore to reach a sufficient signal-
146 to-noise ratio we consider only one average of about 320 spectra acquired from Dec. 2004 and
147 Sept. 2009, encompassing the entire south and mid-latitudes within the range of 90°S to 20°N ;
148 during this time period and at these latitudes data can be considered quite homogeneous as
149 shown in Teanby et al. (2010). We exclude the higher northern latitudes where the stratospheric
150 temperature profile changes significantly. We have also selected data acquired from a Cassini-
151 Titan distance less than 45,000 km in order to limit the size of the projected detector footprint to
152 less than 150 km.

153

154 *3. Data analysis and model*

155

156 Across the considered portion of FP1 spectral range, Titan's spectrum is formed by (i) the
157 contribution of thermal emission of the surface and atmospheric layers, (ii) the seven pairs
158 (Anderson and Samuelson 2011) of collision induced absorption (CIA) opacities between the
159 main atmospheric molecules - nitrogen, methane and hydrogen - due to Titan's dense lower
160 atmosphere, (iii) the photochemical aerosol plus stratospheric condensates, and (iv) the ro-

161 vibrational emission lines corresponding to the emission of atmospheric species present at the
162 latitudes included in our study: CH₄, CO, H₂O, C₄H₂.

163 These quantities were used as input to the NEMESIS retrieval code (Irwin et al. 2008) to perform
164 a combination of correlated-k forward model computation (Lacis and Oinas 1991) and retrieval
165 scheme based on the method of optimal estimation (Rodgers 2000) in order to determine Titan's
166 atmospheric opacity, simulate its emerging radiation field, and retrieve Titan's water vapor
167 abundance. This method was successfully applied to model the FPI spectrum in Cottini et al.
168 (2012) to retrieve surface temperature. A Hamming apodization was used, in keeping with the
169 measured FPI data.

170 We solve the radiative transfer equation for 147 spherical atmospheric layers, using as source
171 function the thermal emission of the surface, for which a unit surface emissivity is assumed, and
172 that of the atmospheric layers. The retrieval algorithm then iteratively computes a synthetic
173 spectrum, compares it to the data and after applying a cost function, determines the best estimate
174 for the physical parameters in the model (the stratospheric aerosol profile and any necessary
175 adjustments to the temperature profile and the mole fraction of included atmospheric gas). The
176 cost function includes two components: one that measures the quality of the fit to the spectra
177 (similar to a χ^2 test) and the other that considers the deviation of the retrieved parameters from a
178 set of *a priori* quantities.

179 We include in the model the CIA of the atmospheric molecules N₂, CH₄ and H₂, which
180 contribute to the opacity affecting the level of the spectrum continuum; they were calculated
181 according to Borysow and Frommhold (1986a) , Borysow and Frommhold (1986b) , Borysow
182 and Frommhold (1986c) and Borysow and Frommhold (1987), Borysow (1991) and Borysow
183 and Tang (1993). For the N₂-CH₄ pair, we have used CIA coefficient values increased by 50% as

184 recommended in Tomasko et al. (2008) and then confirmed in de Kok et al. (2010) based on a
185 comparison between model prediction and the far-infrared continuum data.

186 We have modeled the haze emission/absorption using the extinction cross sections of the hazes
187 included in de Kok et al. (2007b). Since scattering is negligible at these wavelengths for particles
188 smaller than few microns, we have omitted it from our computations.

189 We have adopted the atmospheric vertical temperature–pressure profiles retrieved from CIRS
190 data for three latitudes (15°N, 15°S, 58°S) from Anderson and Samuelson (2011) from the
191 surface to 3.3×10^{-7} bar, corresponding to an altitude range of 0-600 km. Spectroscopic
192 information of the gas rotational lines in the far-infrared range was extracted from the HITRAN
193 2004 database (Rothman et al. 2005). For CH₄ we have adopted the revised mole fraction of 1.48
194 % in the stratosphere (Niemann et al. 2010) acquired by the Gas Chromatograph Mass
195 Spectrometer (GCMS) on the Huygens probe in its descent to Titan's surface. In the stratosphere
196 for H₂ we assumed a uniform volume mixing ratio of 0.1% (Courtin et al. 2008). The geometry
197 of the observations was also included in the computations.

198 An accurate model of the emerging radiation field is required to successfully reproduce CIRS
199 spectra and measure water abundance. The FP1 FOV is circular and has a sensitivity that
200 decreases from the center to the edge (0-3.9 mrad) where it drops to zero. For on-disk spectra the
201 homogeneity of the field of view usually permits simple modeling with a single ray calculated
202 for the detector center. For limb spectra, we have to take into account the rapid decrease in
203 atmospheric density with the height and the variations of temperature and gas volume mixing
204 ratio profile with altitude. In such a case, the FOV is not assumed to be uniform and a multiple
205 ray model is required to fit the data. We modeled the FOV using the minimum number of rays
206 for which the synthetic spectrum and the water retrieval computation results became stable; this

207 corresponds to 9 rays with a step in altitude of 25 km. We also recomputed some of the results
208 using 39 rays (step of 5 km) in order to show a smoother limb contribution function. Spectral
209 radiance measured by the FPI detector is modeled by a convolution of the emerging radiance at
210 each point in the FOV (as described in Nixon et al. 2009a and in Teanby and Irwin 2007),
211 weighted by a Gaussian response function for CIRS FPI detector. This response function – the
212 actual beam profile – was determined for CIRS FPI (Flasar et al. 2004) during Cassini flybys of
213 Jupiter which, due to the large distance of observation, was considered as a point source. As 95%
214 of the integrated response is contained in a radius of 1.95 mrad from the FOV center, the detector
215 observes an actual maximum altitude range of about 70 km.

216 Line-by-line independent calculations to simulate the same on-disk FPI selections were also
217 made using the Atmospheric Radiative Transfer (ART) code used by Coustenis and co-authors in
218 previous papers and more recently applied to CIRS data in Coustenis et al. (2010). The code uses
219 the most recent aerosol extinction dependence inferred from Vinatier et al. (2012) and
220 temperature profiles derived by fitting the ν_4 methane band at 1304 cm^{-1} in FP4 averages taken at
221 similar conditions as the FPI spectra. The spectroscopic parameters for all the observed
222 molecules and isotopes are from GEISA 2009 (Jacquinet et al. 2011) and HITRAN 2008
223 (Rothmann et al. 2009). The results from these two different codes are quite similar and largely
224 within error bars.

225 In Figure 1 (upper panel) the on-disk and two limb observation averages are shown together with
226 their fit. Figure 1 (lower panel) shows only the spectral range used for the water line analysis.

227

228

229

230 4. Results

231

232 We have retrieved water vapor abundance from both on-disk and limb data assuming different
233 water vapor mole fraction dependences on altitude: a constant water mixing ratio profile and
234 three vertical distribution profiles with the mole fraction increasing with height as predicted by
235 recent photochemical models: a) Horst et al. (2008) and b) Wilson and Atreya (2004) and c) Lara
236 et al. (1996), a previous model adopted in Coustenis et al. (1998) for the first water detection by
237 ISO. The constant profile along the atmosphere (*a priori* assumed to be 0.1 ppb) at the altitude
238 where the water vapor freezes is forced to decrease to zero following the saturation law. Using
239 the saturation vapor pressure equation of water over ice of Murphy and Koop (2005) and
240 assuming the temperature profile retrieved at 15° N we find a condensation altitude of about 93
241 km. We have also computed the contribution functions - normalized inversion kernels - showing
242 the sensitivity of each atmospheric layer to a variation of the H₂O mixing ratio. These
243 contribution functions were computed for each profile and for all of the most intense water lines
244 in order to provide an altitude range of validity of the retrieved values (Figure 2 and 3). Figure 2
245 shows the contribution functions for on-disk observations computed at four different wave
246 numbers; at 254 cm⁻¹ (one of the two lines used for the ISO water retrieval) the upper shoulder of
247 the contribution function is wider and sensitive to higher altitudes compared to the other wave
248 numbers used for the water retrieval in this work. In our case the fit of the 254 cm⁻¹ line
249 improves when using a profile increasing with altitude rather than a constant profile. In Figures 3
250 we show only the contribution functions computed at wavenumber 202.75 cm⁻¹, where the most
251 intense water line in the far infrared occurs (discounting the line at 150.5 cm⁻¹ due to enhanced
252 electronic noise).

253 For water retrievals obtained using a constant water profile we show the retrieved mixing ratio
254 values at the altitude where the water functional derivative peaks for the assumed profile (Table
255 1). We associate to this altitude an error equal to the FWHM of the contribution function for the
256 corresponding water profile. We also retrieve a scaling factor to the water profile associated with
257 each of the photochemical model considered in this work (Table 1).

258

259 *4.1 On – disk water retrieval*

260

261 To measure the water abundance from the on-disk average ($0^\circ - 30^\circ$ N) data we first use a
262 constant water profile. We retrieve a volume mixing ratio of (0.14 ± 0.05) ppb for altitudes
263 ranging between ~ 93 and 130 km, where the contribution function peaks at around 97 km. This
264 value corresponds to a surface-normalized H_2O total column density on the order of $(3.7 \pm 1.3) \times$
265 10^{14} molecules/cm².

266 The sensitivity of the retrieved results at the altitude where the water vapor freezes (this strongly
267 depends on the assumed temperature profile and the water mixing ratio) is the most important
268 source of error for the on-disk observations since condensation occurs in the altitude region
269 where the spectrum is sensitive to water vapor. Small variations of the temperature profile in the
270 stratosphere, random noise, and a small dependence in altitude sensitivity with wavenumber are
271 other included sources of error.

272 We also fit the water lines for the three other water vertical distribution profiles (Horst et al.
273 2008, Wilson and Atreya 2004 and Lara et al. 1996) and obtained the necessary scale factors to
274 fit the data, which are shown in Table 1. These values, ranging between 0.11 and 0.63 times the
275 considered profiles, show the retrieved water mole fraction to be less than predicted from these

276 previous models.

277 We have analyzed two additional latitudinal bins from 45°S to 10°S and from 80°S to 45°S,
278 centered on the corresponding temperature profiles retrieved from CIRS, at 15°S and 58°S
279 respectively. The observed water mixing ratio indicates the absence of any significant latitudinal
280 variations within the data uncertainties in the considered latitude range. It should be stressed in
281 fact that in this work we did not analyze the water stratospheric content at high northern latitudes
282 that were experiencing winter during this time period. To model spectra at these latitudes for a
283 large average is particularly complex since the stratospheric temperature change quickly with
284 latitude; besides, a temperature profile for high northern latitudes is not yet available for the
285 stratospheric region where water saturates and to which CIRS on-disk spectra are more sensitive.
286 The results obtained simultaneously for on-disk data only using the independent line-by-line
287 ART code simulations of the same FP1 selections confirm well within the error bars the retrieved
288 water vapor values reported above.

289

290 *4.2 Limb water retrieval*

291

292 The measurement of water vapor obtained by modeling the limb 1 spectrum under the
293 assumption of a constant mixing ratio profile is equal to (0.13 ± 0.04) ppb. This value is relative
294 to an altitude around 115 km according to the position of the peak of the corresponding
295 contribution function.

296 Modeling the limb 2 spectrum we retrieved a water mixing ratio of (0.45 ± 0.15) ppb using a
297 constant water profile. The radiance mostly originates from a region centered at 230 km (190-
298 275 km at half maximum of sensitivity). These values indicate an increase of the water mole

299 fraction with altitude in the stratosphere from 115 km to 230 km of about 3 times. Figure 1
300 depicts a comparison of the strength of the water lines in the spectrum targeted at limb 2 altitude
301 to the ones in the limb 1 spectrum. Water lines have decreased proportionately less in radiance
302 than the methane lines, indicating qualitatively an increase of water with altitude, as methane is
303 uniformly mixed in this range: water lines around 115 km are only 1-2 times stronger than the
304 corresponding lines at 230 km while methane lines are 3-5 times stronger.

305 The scaling factors to the model water profiles obtained from the two types of limb retrievals are
306 shown in Table 1 and again illustrate the smaller amount of stratospheric water vapor detected by
307 CIRS in respect to the one predicted by models.

308

309 *5. Conclusions*

310

311 In this work we modeled CIRS data with a constant-with-height water vapor profile and assigned
312 the retrieved mixing ratio to the altitude where the contribution function peaks.

313 By combined on-disk and limb observations we are able to constrain the vertical profile of water
314 in the region of the stratosphere – from 12 mbar to 10^{-3} mbar, corresponding to altitudes between
315 93 and 280 km (considering the widths of the contribution functions).

316 In Figure 4 we summarize our water vapor retrieved values and infer vertical profiles showing
317 also the models of Horst et al. (2008), Wilson and Atreya (2004) and Lara et al. (1996) for
318 comparison.

319 The measurement of the stratospheric vertical profile of water adds useful constraints to the
320 photochemical models of Titan's atmosphere. The increase of the water mixing ratio with
321 altitude is in agreement with an external source of oxygen and lower altitude a sink due to

322 photolysis and condensation. The abundance instead seems to be less (from ~ 0.1 to ~ 0.6) than
323 predicted from the models considered in this work (see Table 1). We also observe that since the
324 scaling factors to the photochemical models a), b) and c) in Table 1 are more or less different for
325 the two limb altitudes, it implies that these models might have a slope for H₂O not quite
326 consistent with CIRS data. However, due to the quick variation of the water vapor mole fraction
327 with altitude in the atmospheric region where water freezes and where CIRS is actually
328 observing (on-disk and limb 1 spectra), we should be careful in the evaluation of the water
329 profile slope and include the measurements errors to estimate it.

330 ISO retrieved a water vapor abundance of 0.4 ppb assuming a constant mole fraction above the
331 condensation level (Coustenis et al. 1998); we associate to this value the same relative error bars
332 as those derived by ISO for the scaled Lara et al. (1996) profile: the data were fit with a scaling
333 factor to the water profile of $(0.4 +0.3 -0.2)$. From CIRS on-disk observations we retrieved a
334 volume mixing ratio of (0.14 ± 0.05) ppb around 97 km for latitudes ($0^\circ - 30^\circ$ N) which is only
335 marginally consistent with the ISO determination of 0.4 ppb, considering the error bars and the
336 different atmospheric models and geometry of observation of the two instruments.

337 We also fit the CIRS data assuming the water profile from Lara et al. (1996) multiplied for a
338 scaling factor of 0.48 ± 0.07 (corresponding to a water column density of $3.8 \pm 1.0 \times 10^{14}$
339 molecules cm⁻²). This result agrees with the scaling factor of $(0.4 +0.3 -0.2)$ retrieved from ISO
340 observations by Coustenis et al. (1998) but this agreement may be fortuitous as, in the ISO
341 geometry (integrated flux), most of the emission originates from above 300 km with the
342 contribution functions peaking around 400 km (Fig. 3 of Coustenis et al. 1998). This is due to a
343 strong emission from the limb occurring at high altitudes when 0.4 times the Lara et al. (1996)
344 profile is used. In contrast, using this H₂O profile, the contribution functions for the CIRS nadir

345 selection cover the range 95-145 km (at half maximum).

346 In previous photochemical models, as in Lara et al. (1996), in order to include external sources
347 of CO, it was postulated that CO could be produced through a chemical reaction between OH
348 (available from H₂O influx into the upper atmosphere) and CH₃. It was found instead by Wong et
349 al. (2002) that this reaction produces H₂O and not CO as previously assumed.

350 Hence an influx of H₂O or OH does not produce any significant abundance of CO and therefore
351 CO₂ can be produced by an H₂O influx only with CO already present (OH + CO → CO₂ + H).
352 For this reason these models were unable to reproduce the observed CO abundance and were
353 substituted by other models that suggest the existence of primordial CO in the atmosphere
354 (Wilson and Atreya 2004) or consider for CO a solely external origin but this requires an influx
355 of O⁺ rather than H₂O or OH.

356 In the pre-Cassini model of Wilson and Atreya (2004) water is photolyzed to OH, which
357 combines with CO to form CO₂ and other complex species. In this model, CO is assumed to be
358 primordial on Titan and the water abundance profile derives from the amount necessary to form
359 the observed CO₂. This assumption was challenged by the Horst et al. (2008) model, in which
360 oxygen species are assumed to arrive from outside the moon and form carbon monoxide as well
361 as carbon dioxide in the atmosphere. The values of the input fluxes of O and OH were adjusted
362 to reproduce the observed abundances of CO and CO₂. In the Horst et al. (2008) model water
363 profiles were produced for six different values (from $K = 100 \text{ cm}^2 \text{ s}^{-1}$ to $K = 1000 \text{ cm}^2 \text{ s}^{-1}$) of the
364 eddy coefficient in the lower atmosphere, since the stratospheric abundances of photochemically
365 produced species are highly dependent on this parameter. As shown in Fig. 4, the water
366 abundance retrieved in our study is best fit by the water profile with the lowest eddy diffusion
367 coefficient value considered in their model ($K = 100 \text{ cm}^2 \text{ s}^{-1}$), which is far from the value ($K =$

368 400 cm² s⁻¹) they identified as better reproducing CIRS observations of hydrocarbon species and
369 adopted in this work for comparison with our retrievals. Our results show that even the Horst
370 model with K=100 cm² s⁻¹ still has too much water.

371

372 *Acknowledgements*

373

374 Valeria Cottini is supported by the NASA Postdoctoral Program. Thanks to S. Horst, E. Wilson
375 and S. Atreya for providing water profiles for comparison and to Paul Romani for water
376 chemistry discussions. The US-based authors were funded by the NASA Cassini Mission during
377 the period in which this work was performed. N. Teanby was supported by the Leverhulme Trust
378 and the UK Science and Technology Facilities Council.

379

380 *References*

381

382 Anderson, C. M., Samuelson, R. E., Titan's aerosol and stratospheric ice opacities between 18 and 500
383 μm: Vertical and spectral characteristics from Cassini CIRS, 2011. *Icarus*, 212, 762-778

384 Bjoraker, G., Achterberg, R., Anderson, C., Samuelson, R.; Carlson, R.; Jennings, D., 2008. American
385 Astronomical Society, DPS meeting #40, #31.12; Bulletin of the AAS, 40, 448.

386 Borysow, A., 1991. Modelling of collision-induced infrared-absorption spectra of H₂-H₂ pairs in the
387 fundamental band at temperatures from 20 K to 300 K. *Icarus*, 92 (2), 273-279.

388 Borysow, A., Frommhold, L. 1986a. Theoretical collision-induced rototranslational absorption spectra for
389 modeling Titan's atmosphere — H₂-N₂ pairs. *Astrophys. J.*, 303, 495-510.

390 Borysow, A., Frommhold, L. 1986b. Theoretical collision-induced rototranslational absorption spectra for
391 the outer planets — H₂–CH₄ pairs. *Astrophys. J.*, 304, 849–865.

392 Borysow, A., Frommhold, L. 1986c. Collision-induced rototranslational absorption spectra of N₂–N₂ pairs
393 for temperatures from 50 to 300 K. *Astrophys. J.*, 311, 1043–1057.

394 Borysow, A., Frommhold, L. 1987. Collision-induced rototranslational absorption spectra of CH₄–CH₄
395 pairs at temperatures from 50 to 300 K. *Astrophys. J.*, 318, 940–943.

396 Borysow, A. and Tang, C., 1993. Far infrared CIA spectra of N₂–CH₄ pairs for modelling of Titan's
397 atmosphere. *Icarus*, 105, 175–183.

398 Cottini, V., Nixon, C. A., Jennings, D. E., de Kok, R., Teanby, N.A., Irwin, P. G. J., Flasar, F. M., 2012a.
399 Spatial and temporal variations in Titan's surface temperatures from Cassini CIRS observations. *Planet.*
400 *Space Sci.*, 60, 62–71.

401 Courtin, R.D., Sim, C., Kim, S., Gautier, D., Jennings, D.E., 2008. Latitudinal variations of tropospheric
402 H₂ on Titan from the Cassini CIRS investigation. *Bull. Am. Astron. Soc.*, 40, 446.

403 Coustenis, A., Encrenaz, Th., Bézard, B., Bjoraker, Graner, G., Dang-Nhu, M., Arié, E., 1993. Modeling
404 Titan's thermal infrared spectrum for high-resolution space observations. *Icarus*, 102, 240-260.

405 Coustenis, A.; Salama, A.; Lellouch, E.; Encrenaz, Th.; Bjoraker, G. L.; Samuelson, R. E.; de Graauw,
406 Th.; Feuchtgruber, H.; Kessler, M. F., 1998. Evidence for water vapor in Titan's atmosphere from
407 ISO/SWS data. *A&A*, 336, L85-L89.

408 Coustenis, A. et al., 2007. The composition of Titan's stratosphere from Cassini/CIRS mid-infrared
409 spectra. *Icarus*, 189, 35-62.

410 Coustenis, A. et al., 2010. Titan trace gaseous composition from CIRS at the end of the Cassini-Huygens
411 prime mission. *Icarus*, 207, 461-476.

412 de Kok, R. Et al., 2007a. Oxygen compounds in Titan's stratosphere as observed by Cassini CIRS. *Icarus*,
413 186, 354-363.

414 de Kok, R., Irwin, P.G.J., Teanby, N.A., 2010. Far-infrared opacity sources in Titan's troposphere
415 reconsidered. *Icarus*, 209 (2), 854–857.

416 Dougherty, M. K., Khurana, K. K., Neubauer, F. M., Russell, C. T., Saur, J., Leisner, J. S. and Burton,
417 M. E., 2006. Identification of a Dynamic Atmosphere at Enceladus with the Cassini Magnetometer.
418 *Science*, 311, 1406-1409.

419 English, M. A.; Lara, L. M.; Lorenz, R. D.; Ratcliff, P. R.; Rodrigo, R., 1996. Ablation and chemistry of
420 meteoric materials in the atmosphere of Titan. *ASR*, 17, 157-160.

421 Flasar, F. M., and 44 colleagues, 2004. Exploring the Saturn system in the thermal infrared: The
422 Composite Infrared Spectrometer. *Space Sci. Rev.*, 115, 169 – 297.

423 Gurwell, Mark A. 2004. Submillimeter Observations of Titan: Global Measures of Stratospheric
424 Temperature, CO, HCN, HC₃N, and the Isotopic Ratios ¹²C/¹³C and ¹⁴N/¹⁵N. *Astrophys. J.*, 616, L7-L10.

425 Hartle, R. E., et al. (2006a), Preliminary interpretation of Titan plasma interaction as observed by the
426 Cassini Plasma Spectrometer: Comparisons with Voyager 1, *Geophys. Res. Lett.*, 33.

427 Hartle, R. E., et al. (2006b), Initial interpretation of Titan plasma interaction as observed by the Cassini
428 Plasma Spectrometer: Comparisons with Voyager 1, *Planet. Space Sci.*, 54, 1211.

429 Hartogh, P.; Lellouch, E.; Moreno, R.; Bockelée-Morvan, D.; Biver, N.; Cassidy, T.; Rengel, M.;
430 Jarchow, C.; Cavalié, T.; Crovisier, J.; Helmich, F. P.; Kidger, M., 2011. Direct detection of the
431 Enceladus water torus with Herschel. *A&A*, 532, id.L2.

432 Hidayat, T.; Marten, A.; Bezaud, B.; Gautier, D.; Owen, T.; Matthews, H. E.; Paubert, G., 1998.
433 Millimeter and Submillimeter Heterodyne Observations of Titan: The Vertical Profile of Carbon
434 Monoxide in Its Stratosphere. *Icarus*, 133, 109-133.

435 Hörst, S. M.; Vuitton, V.; Yelle, R. V., 2008. Origin of oxygen species in Titan's atmosphere. *J. Geophys.*
436 *Res.*, 113, E10.

437 Irwin, P.G.J., Teanby, N.A., de Kok, R., Fletcher, L.N., Howett, C.J.A., Tsang, C.C., Wilson, C.F.,
438 Calcutt, S.B., Nixon, C.A., Parrish, P.D., 2008. The NEMESIS planetary atmosphere radiative transfer
439 and retrieval tool. *J. Quant. Spectrosc. Radiat. Trans.*, 109, 1136-1150.

440 Jacquinet-Husson, N., et al., 2011. The 2009 edition of the GEISA spectroscopic database. *JQSRT*, 112,
441 2395-2445.

442 Lacis, A.A., and V. Oinas, 1991. A description of the correlated k distributed method for modeling
443 nongray gaseous absorption, thermal emission, and multiple scattering in vertically inhomogeneous
444 atmospheres. *J. Geophys. Res.*, 96, 9027-9063.

445 Lara, L. M., Lellouch, F., Lopez-Moreno, J. J., & Rodrigo, R. 1996, *J. Geophys. Res.*, 101, 23,261.

446 Lutz, B. L.; de Bergh, C.; Owen, T., 1983. Titan - Discovery of carbon monoxide in its atmosphere.
447 *Science*, 220, 1374, 1375.

448 Murphy, D. M. and Koop, T., 2005. Review of the vapour pressures of ice and supercooled water for
449 atmospheric applications. *QJRMS*, 131, 1539–1565.

450 Niemann, H. B., et al., 2010. The composition of Titan's lower atmosphere and simple surface volatiles as
451 measured by the Cassini-Huygens probe gas chromatograph mass spectrometer experiment, *J. Geophys.*
452 *Res.*, 115, pp. E12006.

453 Nixon, C. A., Teanby, N. A., Calcutt, S. B., Aslam, S., Jennings, D. E., Kunde, V.G., Flasar, F. M., Irwin,
454 P. G., Taylor, F. W., Glenar, D. A., and Smith, M. D., 2009a. Infrared limb sounding of Titan with the
455 Cassini Composite InfraRed Spectrometer: effects of the mid-IR detector spatial responses. *Appl. Opt.* 48,
456 1912-1925.

457 Rodgers, C. D., 2000. *Inverse Methods for Atmospheric Sounding: Theory and Practice*. World
458 Scientific, Singapore.

459 Rothman L.S. et al. 2005. The HITRAN 2004 molecular spectroscopic database. *J. Quant. Spectrosc.*
460 *Radiat. Trans.*, 96, 139–204.

461 Rothman, L.S., Gordon, I.E. et al, 2009. The HITRAN 2008 Molecular Spectroscopic Database, *J. Quant.*
462 *Spectrosc. and Rad. Transfer*, 110, 533-572.

463 Samuelson, R. E.; Maguire, W. C.; Hanel, R. A.; Kunde, V. G.; Jennings, D. E.; Yung, Y. L.; Aikin, A. C.
464 , 1983. CO₂ on Titan. *J. Geophys. Res.*, 88, 8709-8715.

465 Teanby, N. A.; Irwin, P.G.J.; de Kok, R.; Jolly, A.; Bézard, B.; Nixon, C. A.; Calcutt, S. B., 2009. Titan's
466 stratospheric C₂N₂, C₃H₄, and C₄H₂ abundances from Cassini/CIRS far-infrared spectra. *Icarus*, 202, 620-
467 631.

468 Teanby, N. A. and P. G. J. Irwin, 2007. "Quantifying the effect of finite field-of-view size on radiative
469 transfer calculations of Titan's limb spectra measured by Cassini-CIRS," *Astrophys. Space Sci.* 310, 293-
470 305.

471 Tomasko, M. G.; Bézard, B.; Doose, L.; Engel, S.; Karkoschka, E.; Vinatier, S., 2008. Heat balance in
472 Titan's atmosphere. *Planet. Space Sci.*, 56, 648-659.

473 Vinatier, S., Rannou, P., Anderson, C.M., Bézard, B., de Kok, R., Samuelson, R.E., 2012. Optical
474 constants of Titan's stratospheric aerosols in the 70-1500 cm⁻¹ spectral range constrained by Cassini/CIRS
475 observations. *Icarus* 219, 5-12.

476 Wilson, E. H.; Atreya, S. K. 2004, Current state of modeling the photochemistry of Titan's mutually
477 dependent atmosphere and ionosphere. *J. Geophys. Res.*, 109, E6.

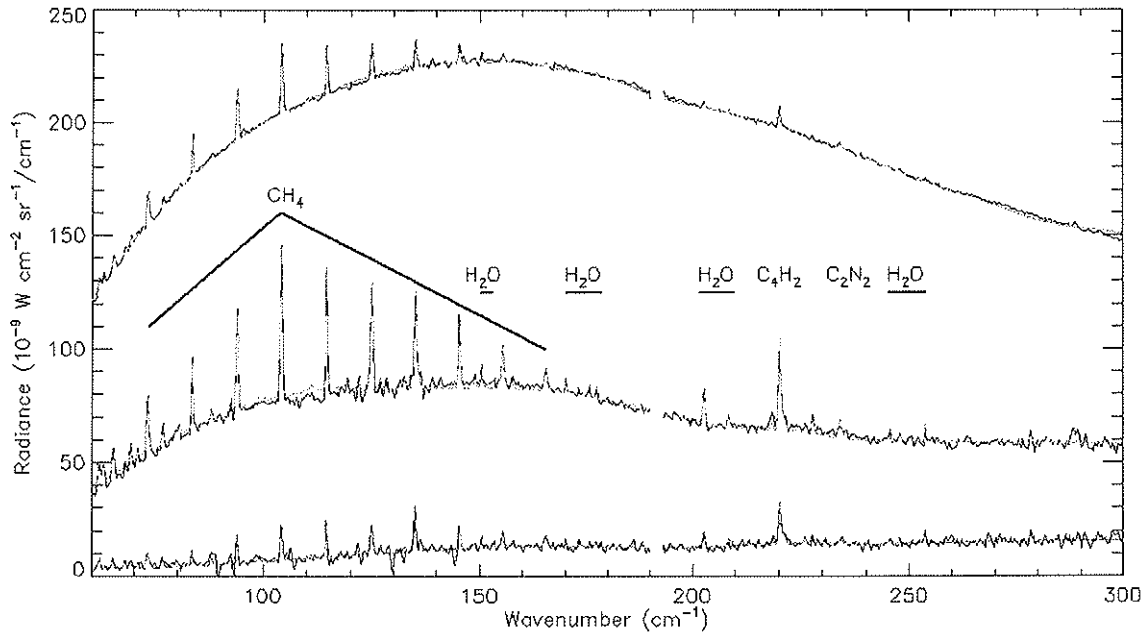
478 Wong, A., Morgan, C. G., Yung, Y. L., Owen, T. 2002, Evolution of CO on Titan. *Icarus*, 155, 2, 382-
479 392.

480

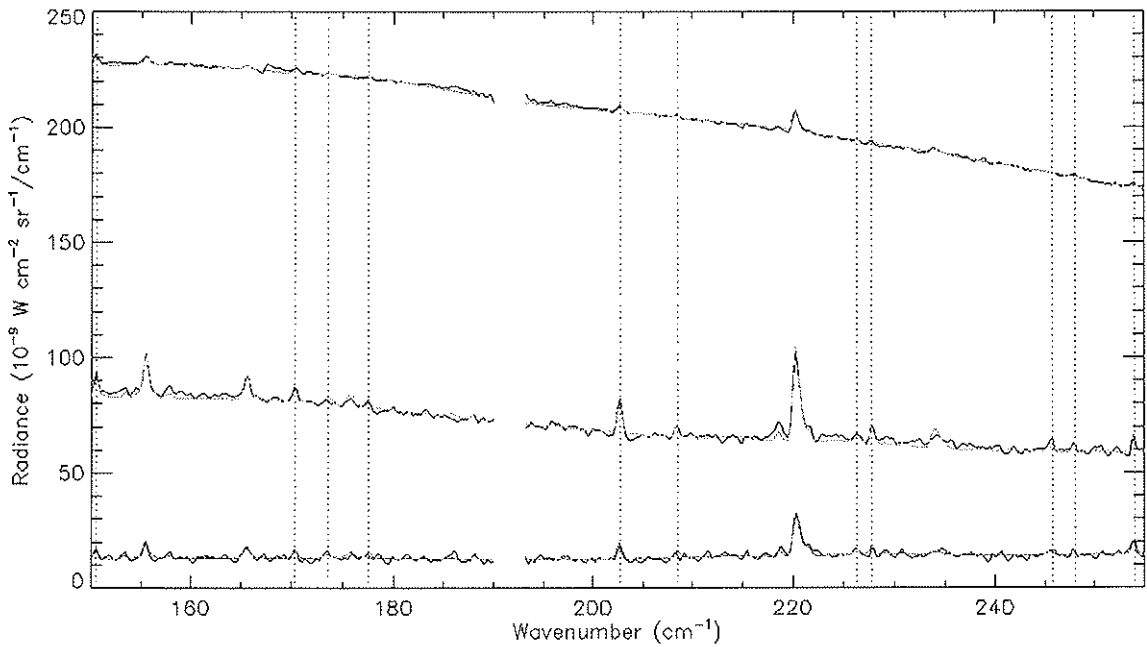
481

482

483



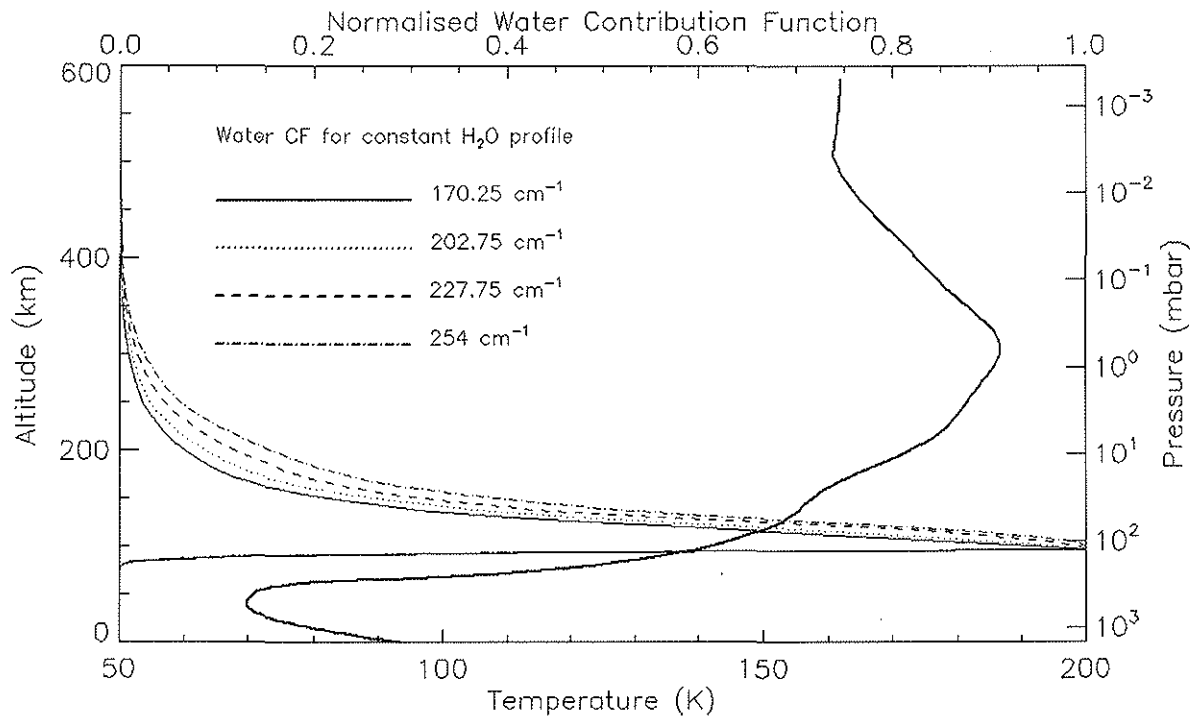
484



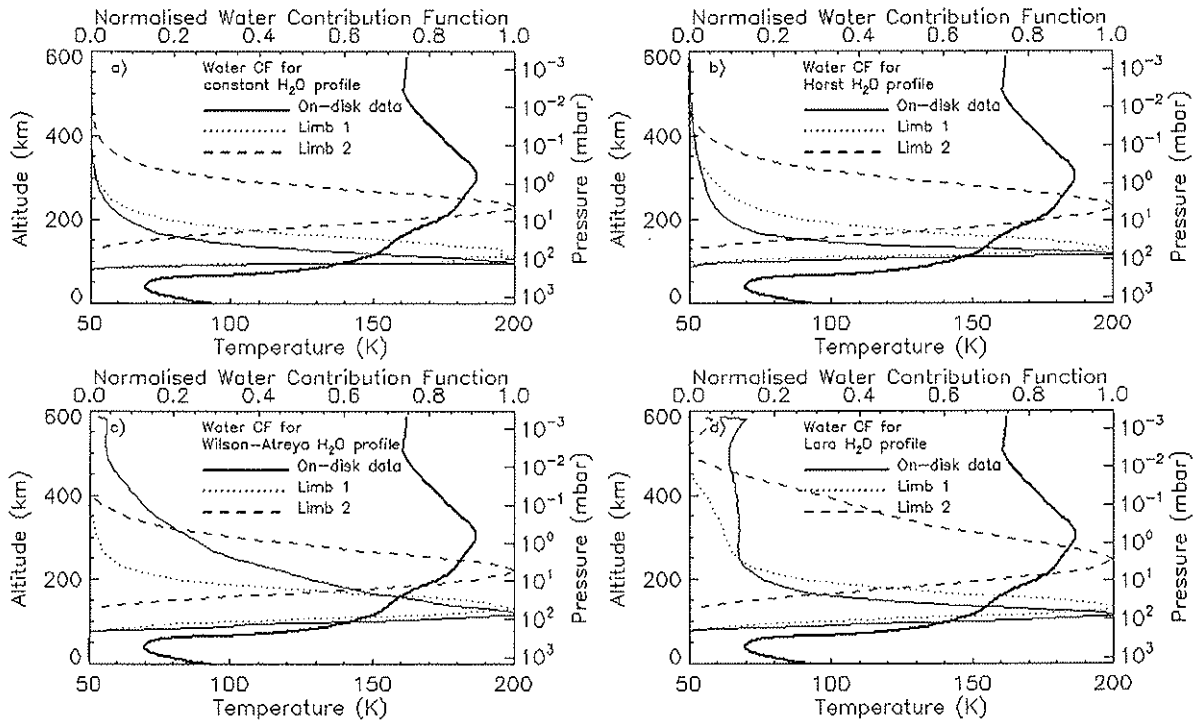
485

486 Figure 1. Upper panel: In black, the average of CIRS far-IR on-disk observations is plotted

487 (~7,000 spectra acquired from Dec. 2004 to Dec. 2008 in the latitudinal range of (0° – 30° N),
 488 limb observations centered around 115 and 230 km (respectively ~320 and ~280 spectra acquired
 489 from Dec. 2004 to Sep. 2009 in the latitudinal range of 90°S– 20°S) and their fit (in green, blue,
 490 red respectively) assuming a constant water mole fraction above the condensation altitude.
 491 Lower panel: the retrieval spectral range is shown with the main water lines indicated by vertical
 492 dotted lines.
 493



494
 495 Figure 2. Contribution functions of the different atmospheric layers to the water vapor line
 496 emission computed for four wave numbers. In solid line is shown also a temperature profile.

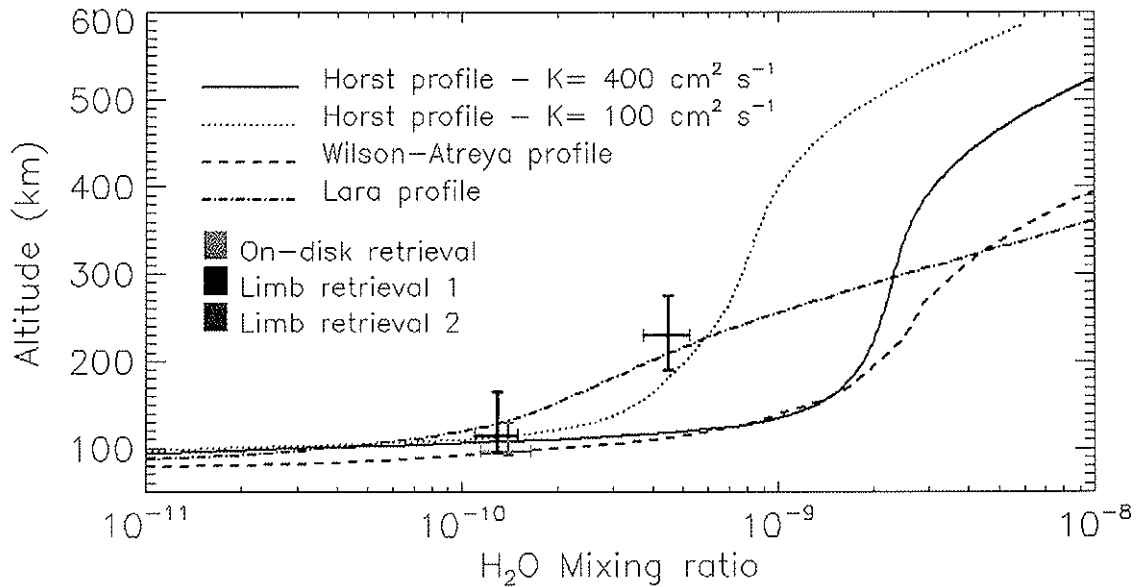


497

498

499 Figure 3. Contribution functions of water vapor line emission and temperature profile. In Figures
 500 3 a,b,c,d we show the contribution functions computed at 202.75 cm^{-1} for different water profile
 501 models: (a) a constant water vertical profile; (b) profile from Horst et al. (2008); (c) profile from
 502 Wilson and Atreya (2004) and (d) profile from Lara et al. (1996).

503



504

505 Figure 4. Water vapor mole fraction retrieved from CIRS on-disk and two limb observations
 506 assuming a water profile constant with altitude over the condensation level. Water profiles from
 507 photochemistry models are also shown for comparison: Horst et al. (2008) water vapor profile
 508 derived assuming two different eddy diffusion coefficients - $100 \text{ cm}^2 \text{ s}^{-1}$ and $400 \text{ cm}^2 \text{ s}^{-1}$ (the
 509 second being the one recommended in their model; dotted curve plus solid curve), the profile in
 510 Wilson and Atreya (2004; dashed curve) and in Lara et al. (1996; dot-dash curve).

511

512

513

514

515

Water Vapor Retrieved Mole Fractions	On-disk Average (0°– 30°)N	Limb Retrieval 1	Limb Retrieval 2
Constant VMR Profile	(0.14 ± 0.05) ppb at (97 + 33 – 4) km	(0.13 ± 0.04) ppb at (115 + 50 – 20) km	(0.45 ± 0.15) ppb at (230 + 45 – 40) km
Scaling Factor to H₂O Profile from Horst	0.18 ± 0.05 at (118 + 20 – 12) km	0.14 ± 0.05 at (129 + 45 – 17) km	0.23 ± 0.07 at (232 + 67 – 60) km
Scaling Factor to H₂O Profile from Wilson-Atreya	0.14 ± 0.05 at (118 + 85 – 22) km	0.13 ± 0.05 at (129 + 46 – 24) km	0.18 ± 0.08 at (222 + 62 – 53) km
Scaling Factor to H₂O Profile from Lara	0.48 ± 0.07 at (115 + 20 – 30) km	0.63 ± 0.07 at (133 + 42 – 27) km	0.45 ± 0.08 at (247 + 33 – 100) km

516

517 Table 1. Retrieval of water abundance from on-disk observations (0°– 30°) N and from limb
518 observations targeted at two altitudes assuming a constant water mixing ratio over the
519 condensation region (second row). The altitude associated with the retrieval and its error is given
520 by respectively the peak and the FWHM of the contribution function relative to the assumed
521 water profile. In the subsequent rows are shown the retrieved scaling factor to water profiles
522 given in the models of Horst et al. (2008), which assumes $K = 400 \text{ cm}^2 \text{ s}^{-1}$, Wilson and Atreya
523 (2004) and Lara et al. (1996).